



Inertial focusing in planar pulsatile flows

Giridar Vishwanathan¹ and Gabriel Juarez^{1,†}

¹Department of Mechanical Science and Engineering, University of Illinois at Urbana–Champaign, Urbana, IL 61801, USA

(Received 20 March 2021; revised 22 April 2021; accepted 9 May 2021)

Oscillatory flows have the potential to overcome long-standing limitations encountered when using steady flows for inertial focusing due to low particle Reynolds numbers. The periodic displacement generated by oscillatory flow increases the total path length travelled by a suspended particle with no net displacement within a channel or the need for increased channel length. The effects of unsteady inertial forces on inertial focusing, however, have not been thoroughly examined. Here, we present a combined theoretical and experimental study on the effect of Womersley number on inertial focusing in planar pulsatile flows. The migration velocity for a small and weakly inertial particle was evaluated for different oscillation frequencies using the method of matched asymptotics. Using experiments in a custom-built microchannel, we show that oscillatory flows are remarkably efficient for inertial focusing, even at low particle Reynolds numbers. For appropriately selected oscillation amplitude and frequency, inertial focusing is achieved in only a fraction of the channel length (1 % to 10 %) compared to what would be required in a steady flow. We show that the Womersley number influences the equilibrium focusing position and the overall focusing efficiency. In fact, above a critical Womersley number, inertial focusing does not occur despite increasing particle Reynolds number. Lastly, the application of oscillatory inertial focusing for the direct measurement of particle migration velocity is demonstrated.

Key words: microfluidics, particle/fluid flow, suspensions

1. Introduction

Inertial focusing refers to the migration of finite-sized particles across streamlines to well-defined equilibrium positions in the flow (Segré & Silberberg 1961; Di Carlo *et al.* 2007). Recently, the phenomenon has received significant attention because of its applications in the biomedical field, made possible by advances in microfluidics and microfabrication. The forces responsible for particle migration are entirely hydrodynamic

† Email address for correspondence: gjuarez@illinois.edu

in origin and increase proportionally with flow velocity, thus facilitating high-throughput applications without the need for microscale actuators. Inertial focusing is most commonly used for separation of particles based on biomarkers such as size, shape or deformability, particularly as it relates to cancer cells, platelets or bacterial cells from blood samples. Other applications include precise sheathless alignment of particles, enrichment of dilute samples and particle exchange across solvents without mixing (Martel & Toner 2014).

The archetypal inertial focusing system consists of a suspension of particles that are uniformly dispersed at the inlet, undergoing steady laminar flow through a long straight channel. At the outlet, suspended particles are no longer uniformly dispersed, but rather exit the channel at well-defined equilibrium positions in the flow. The exact focusing positions are specific to parameters such as the particle Reynolds number (Re_p), particle characteristics (relative size, shape and deformability), channel cross-sectional geometry and fluid rheology (Stoecklein & Di Carlo 2019). For the case of a rigid sphere suspended in an incompressible Newtonian liquid undergoing steady laminar flow, the primary design parameter is the average distance travelled by a particle before it reaches the equilibrium position. The necessary distance to be travelled is estimated by the relation $L_f = \pi D_h / Re_p C_\ell$, where D_h is the hydraulic diameter and C_ℓ is the lift coefficient (Di Carlo 2009). For successful focusing to occur, the channel length must satisfy $L > L_f$, which implies long channel lengths ($L > 15$ cm) for small particles in low- Re flows ($Re_p < 0.1$).

In practical applications, channel lengths for focusing in steady flows can be reduced by increasing Re_p , which involves an increased flow velocity, larger particles (>5 μm) or narrow channels. For focusing in unsteady flows, however, channel lengths can be reduced by implementing an oscillatory flow component. The periodic displacement generated by the oscillatory component increases the path length travelled within a finite channel to be effectively infinite, given the oscillation frequency, amplitude and number of oscillations. Recently, particles as small as 0.5 μm ($Re_p \approx 0.005$) were successfully focused in short channels using large-amplitude low-frequency oscillatory flows (Mutlu, Edd & Toner 2018). While inertial focusing in unbounded and wall-bounded steady flows are conceptually well understood and have been thoroughly reviewed (Stoecklein & Di Carlo 2019; Shi & Rzehak 2020), inertial focusing in oscillatory flows, specifically the effect of unsteady inertial effects on particle migration velocity, are comparatively unknown (Morita, Itano & Sugihara-Seki 2017).

Early attempts towards the problem of time-dependent lift were first made theoretically for a rigid sphere at small Re_p in an oscillatory simple shear flow (Miyazaki, Bedeaux & Avalos 1995; Asmolov & McLaughlin 1999), and later for flow in a rotating cylinder (Coimbra & Kobayashi 2002). Several parallel numerical studies have addressed time-dependent lift on a sphere in steady shear flow at intermediate Re_p (Wakaba & Balachandar 2005, and references therein). Lift due to oscillatory flow was first studied numerically near a no-slip wall (Fischer, Leaf & Restrepo 2002, 2004). Unlike previous studies, only the work of Fischer *et al.* (2002, 2004) obtains a finite time-averaged lift on the sphere even though the driving shear flow is purely oscillatory, and this is therefore directly relevant to the present study.

Here, we present a combined theoretical and experimental study on the effect of Womersley number on inertial focusing in planar pulsatile flows. The analysis of migration velocity for a small and weakly inertial particle placed in a purely oscillatory channel flow was completed using the method of matched asymptotics. Complementary experiments were performed in a custom-built microfluidic system with an external oscillatory driver, which was used to generate a purely two-dimensional (2-D) pulsatile flow over a

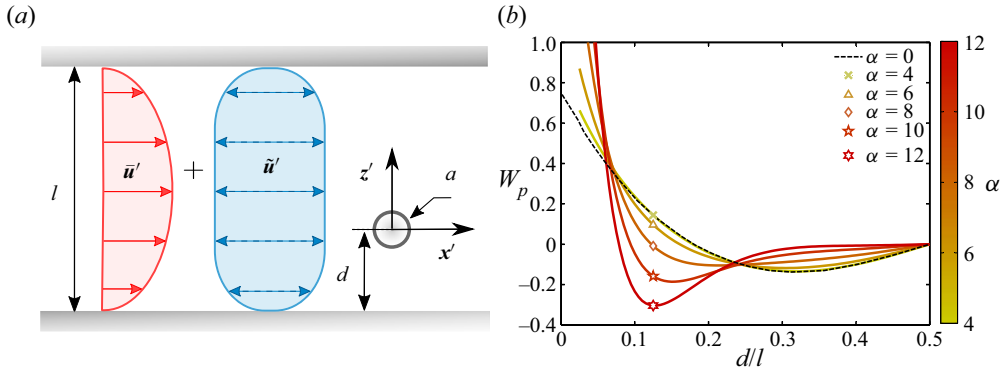


Figure 1. (a) Idealized illustration of inertial focusing in planar pulsatile flows between parallel plates. A spherical particle of radius a is suspended in a pulsatile flow, composed of a steady ($\bar{u}'(z')$) and an oscillatory ($\tilde{u}'(z', t')$) component. (b) Analytical results, (3.18) and (3.19), of the migration velocity profile along the channel width for different Womersley number pulsatile flows.

range of oscillation amplitudes and frequencies. Theoretical results and experimental measurements of focusing position were compared and found to be in good agreement, in the limit of small particles, over a range of Womersley numbers. Finally, the focusing efficiency was characterized for a range of oscillation amplitudes and frequencies using experiments, which determined that, above a critical Womersley number, the focusing efficiency decreased.

2. Problem formulation

Consider the flow configuration illustrated in figure 1(a). A neutrally buoyant spherical particle of radius a is suspended in a Newtonian liquid of kinematic viscosity ν as it flows through a 2-D channel of width l at a distance d from the wall. The underlying flow in the channel is pulsatile and consists of a weak steady flow component $\bar{u}'(z')$ with centreline velocity \bar{u}'_s and a strong oscillatory flow component $\tilde{u}'(z', t')$ with centreline displacement amplitude s and angular frequency ω . The origin of the coordinate system is taken at the centre of the particle.

The relevant non-dimensional numbers are the relative particle size $\kappa = a/l$, the Strouhal number $St = l/s$ and the relative magnitude of the steady flow $\bar{u}'_s/s\omega$. Of primary interest are the channel Womersley number, $\alpha = l\sqrt{\omega/\nu}$, which is a relative measure of the unsteady inertial force to the viscous force, and the particle Reynolds number, $Re_p = a^2s\omega/l\nu = \kappa^2\alpha^2/St$, which quantifies the ratio of the particle's lateral migration velocity to its disturbance velocity. The Reynolds number ($Re = s\omega l/\nu = \alpha^2/St$) quantifies the inertial to viscous forces at the channel scale. It determines focusing position in steady flows, particularly when $Re > 15$ (Segré & Silberberg 1961; Schonberg & Hinch 1989). Here, the isolated effect of oscillatory flow is studied by maintaining $Re < 10$ and varying α . As will be demonstrated, both Re and Re_p are insufficient for describing oscillatory flow focusing. Instead St and α must be considered separately, since they result in qualitatively different effects, especially if $\alpha > 5$.

3. Asymptotic analysis

The treatment here is for a small particle ($Re_p \ll 1$ and $a/l \ll 1$) in a steady 2-D channel flow (Schonberg & Hinch 1989) and is extended to the case of a harmonic purely

oscillatory flow. For a particle with a certain translation velocity U'_p and angular velocity Ω'_p , the governing equations in terms of the position r' , time t' , disturbance velocity u' and disturbance pressure p' are

$$\nabla' \cdot u' = 0, \tag{3.1}$$

$$\nu \nabla'^2 u' - \frac{1}{\rho} \nabla' p' = \partial_{t'} u' + \tilde{u}' \cdot \nabla' u' + u' \cdot \nabla' \tilde{u}' + u' \cdot \nabla' u' + U'_p \cdot \nabla' u'. \tag{3.2}$$

The undisturbed velocity is $\tilde{u}' = s\omega(\tilde{u}e^{i\omega t'} + \tilde{u}^*e^{-i\omega t'})e_x$, where \tilde{u} and its complex conjugate \tilde{u}^* are obtained by applying $z' = \check{z}' + l/2 - d$ and $\tilde{u}(z') = \tilde{u}^\dagger(\check{z}') - \tilde{u}^\dagger(-l/2 + d)$ to the standard pulsatile flow profile for walls at $\check{z}' = \pm l/2$:

$$\tilde{u}^\dagger = \frac{\cosh(\sqrt{i}\alpha\check{z}'/l) - \cosh(\sqrt{i}\alpha/2)}{2(1 - \cosh(\sqrt{i}\alpha/2))}. \tag{3.3}$$

The transformations arise from placing the origin on a particle moving with the flow at a distance d/l from the channel wall, leading to

$$\tilde{u} = \frac{\sinh(\sqrt{i}\alpha\check{z}'/2l) \sinh(\sqrt{i}\alpha(z' + 2d - l)/2l)}{1 - \cosh(\sqrt{i}\alpha/2)}. \tag{3.4}$$

The above equations are subject to a no-slip condition at the particle surface and the channel walls as well as regularity at the far field. That is, $u' = U'_p + \Omega'_p \times r' - \tilde{u}'$ on $r' = a$, $u' = 0$ on $z' = l$ and $z' = l - d$, and finally $u' \rightarrow 0$ as $x' \rightarrow \infty$, respectively.

3.1. Inner problem

For the inner problem, the dimensionless position, time and rate of strain are defined as $r = r'/a$, $t = t'\omega$ and $\gamma = \gamma'(l/s\omega)$, respectively. The corresponding rescaled pressure and velocities are $p = p'(l/\rho\nu s\omega)$, $u = u'(l/s\omega a)$, $U_p = U'_p(l/s\omega a)$ and $\Omega_p = \Omega'_p(l/s\omega)$. The undisturbed velocity is approximated by an oscillatory simple shear flow ($\tilde{u}_l = \gamma z e^{it} e_x + \gamma^* z e^{-it} e_x$), where

$$\gamma = \frac{\sqrt{i}\alpha \sinh(\sqrt{i}\alpha(2d - l)/2l)}{2(1 - \cosh(\sqrt{i}\alpha/2))}. \tag{3.5}$$

The momentum equations become

$$\nabla^2 u - \nabla p = Re_p(St \partial_t u + \tilde{u}_l \cdot \nabla u + u \cdot \nabla \tilde{u}_l + u \cdot \nabla u + U_p \cdot \nabla \tilde{u}_l). \tag{3.6}$$

The boundary conditions for the inner problem are $u = U_p + \Omega_p \times r - \tilde{u}_l$ on $r = 1$ and $u \rightarrow 0$ as $r \rightarrow \infty$. The unsteady term is significant at leading order only if $Re_p St > 1$. Since this is not the case in experiments, this term is neglected, and the equations are identical to those of the inner problem in Schonberg & Hinch (1989). Consequently, the inner problem is quasi-steady, and unsteadiness at the channel scale manifests at the particle scale only through the local shear rate. The solution at the far field ($r \rightarrow \infty$) is

$$u = -\frac{5}{2}(\gamma e^{it} + \gamma^* e^{-it}) \frac{r x z}{r^5} + O(r^{-3}). \tag{3.7}$$

3.2. *Outer problem*

For the outer problem, the dimensionless time and rate of strain are the same as before, while the position is defined as $R = r'/l$. Dimensionalizing (3.7) and rescaling the coordinates with l , we find that the asymptotic matching condition for the disturbance velocity implies that $u' \sim \kappa^3 s\omega$ as $R \rightarrow 0$. It therefore follows that $U = u' / (\kappa^3 s\omega)$, $\tilde{U} = \tilde{u}' / (s\omega)$ and $P = p' (l / \rho \nu s\omega \kappa^3)$. The rescaled momentum equation is

$$\begin{aligned} &\nabla^2 U - \nabla P - \alpha^2 \partial_t U \\ &= Re(\tilde{U} \cdot \nabla U + U \cdot \nabla \tilde{U}) + \frac{10\pi}{3} (\gamma e^{it} + \gamma^* e^{-it}) (e_x \partial_Z + e_z \partial_X) \delta_R, \end{aligned} \quad (3.8)$$

subject to $U = 0$ at $Z = -d/l$ and $Z = 1 - d/l$ as well as $U \rightarrow 0$ as $X \rightarrow \infty$.

The last term on the right-hand side of (3.8) is the singularity at $R = 0$ due to the particle. The contributions of $u' \cdot \nabla' u'$ and $U'_p \cdot \nabla' \tilde{u}'$ are less than the remaining terms by a factor of at least κ^2 and are hence neglected at this order. The equations for a steady flow can be recovered setting $t = 0$ and $\alpha \rightarrow 0$ throughout.

In order to proceed, it is necessary to decouple the time-dependent forcing in (3.8) from the inertial terms for tractability. To do this, a simplifying assumption that $\kappa^2 \ll Re \ll 1$ is made. Although $Re \sim 10$ for our experiments, the assumption is not thought to affect comparison with experiments. This is suggested by the steady flow case, where results derived assuming $Re \ll 1$ in Ho & Leal (1974) are valid at least till $Re = 15$. Next, we choose the following ansatz for U and P :

$$\left. \begin{aligned} U &= U_0 e^{it} + U_0^* e^{-it} + Re(U_{1s} + U_1 e^{i2t} + U_1^* e^{-i2t}) + Re^2(\dots), \\ P &= P_0 e^{it} + P_0^* e^{-it} + Re(P_{1s} + P_1 e^{i2t} + P_1^* e^{-i2t}) + Re^2(\dots). \end{aligned} \right\} \quad (3.9)$$

With the above, the time dependence of U and P has been made explicit. That is, all the newly defined U_i and P_i terms are independent of time. This implies that only U_{1s} and P_{1s} are relevant to long-term particle migration, with the rest averaging out to zero over a single oscillation cycle. The ultimate objective is therefore the evaluation of $U_{1s}(0) \cdot e_z$, which directly yields the particle migration velocity in the laboratory frame. The oscillatory nature of forcing, however, requires U_0 and P_0 to be evaluated first. Substituting the ansatz in (3.8), the $O(1)$ terms give

$$(\nabla^2 - i\alpha^2)U_0 - \nabla P_0 = \frac{10\pi}{3} \gamma (e_x \partial_Z + e_z \partial_X) \delta_R, \quad (3.10)$$

$$\nabla^2 P_0 = -\frac{20\pi}{3} \gamma \partial_X \partial_Z \delta_R. \quad (3.11)$$

The above system of partial differential equations are converted into a system of ordinary differential equations through a Fourier transformation defined as

$$\hat{U}_0(k_1, k_2, Z) = \frac{1}{4\pi^2} \int_{-\infty}^{\infty} \int_{-\infty}^{\infty} U_0 \exp(-i(k_1 X + k_2 Y)) dX dY. \quad (3.12)$$

To obtain cross-stream migration, it is sufficient to consider only the Z component $W_0 = U_0 \cdot e_z$. Equations (3.10) and (3.11) in Fourier space are therefore

$$(d_Z^2 - k^2 - i\alpha^2)\hat{W}_0 - d_Z \hat{P}_0 = 0, \quad (3.13)$$

$$(d_Z^2 - k^2)\hat{P}_0 = 0, \quad (3.14)$$

where $k^2 = k_1^2 + k_2^2$. The boundary conditions are $\hat{W}_0 = 0$ and $d_Z \hat{W}_0 = 0$ at $Z = -d/l$ and $Z = 1 - d/l$. The condition at $Z = 0$ is written as

$$\begin{pmatrix} \hat{P}_0 & d_Z \hat{P}_0 & \hat{W}_0 & d_Z \hat{W}_0 \end{pmatrix}_{0^-}^{0^+} = \frac{5}{6\pi} i k_1 \gamma \begin{pmatrix} 2 & 0 & 0 & 1 \end{pmatrix}. \tag{3.15}$$

To obtain the equations for U_{1s} , the $O(Re)$ terms obtained by substituting the ansatz in (3.8) are gathered and averaged over a single time period. The resulting equation and its divergence are

$$\nabla^2 U_{1s} - \nabla P_{1s} = (W_0 \partial_Z \tilde{U}^* + W_0^* \partial_Z \tilde{U}) e_x + (\tilde{U}^* \partial_X U_0 + \tilde{U} \partial_X U_0^*), \tag{3.16}$$

$$\nabla^2 P_{1s} = -2(\partial_X W_0 \partial_Z \tilde{U}^* + \partial_X W_0^* \partial_Z \tilde{U}). \tag{3.17}$$

The Fourier transforms of the above equations give

$$(d_Z^2 - k^2) \hat{W}_{1s} - d_Z \hat{P}_{1s} = i k_1 (\hat{W}_0 \tilde{U}^* - \hat{W}_0^* \tilde{U}), \tag{3.18}$$

$$(d_Z^2 - k^2) \hat{P}_{1s} = -2i k_1 (\hat{W}_0 d_Z \tilde{U}^* - \hat{W}_0^* d_Z \tilde{U}). \tag{3.19}$$

Note that forcing occurs due to $O(1)$ solutions interacting with the undisturbed flow. At this order, the boundary conditions at $Z = -d/l$ and $Z = 1 - d/l$ are $\hat{W}_{1s} = 0$ and $d_Z \hat{W}_{1s} = 0$. At $Z = 0$, \hat{P}_{1s} and \hat{W}_{1s} along with the corresponding first derivatives are continuous.

3.3. Evaluation of the migration velocity profile

From the exact solutions to (3.13), (3.14), (3.18) and (3.19), the lateral migration velocity can be synthesized numerically using

$$W_p = W_{1s}(0) = \int_{-\infty}^{\infty} \int_{-\infty}^{\infty} \hat{W}_{1s}(0, k_1, k_2) dk_2 dk_1. \tag{3.20}$$

Since \hat{W}_{1s} is even in both k_1 and k_2 , the integration can be limited to the first quadrant so long as the result is multiplied by a factor of 4. To assist convergence of the integral, the analytical solution for $k \gg 1$ was used:

$$\hat{W}_{1s}(0) = \frac{15k_1^2 \alpha^2}{64\pi k^5} \operatorname{Re} \left[\frac{i\gamma \cosh(i^{3/2} \alpha (d/l - 1/2))}{\cosh(i^{3/2} \alpha / 2) - 1} \right], \tag{3.21}$$

where Re denotes the real part.

The variation of the particle migration velocity W_p with d/l for different values of the Womersley number is shown in figure 1(b). For small Womersley numbers ($\alpha \leq 5$), the migration velocity profiles are very similar to one another and, more importantly, nearly identical to the migration profile expected for steady flow, within a numerical factor of exactly 1/2 (Asmolov 1999). The factor of 1/2 arises from the time average of the $\cos^2 t$ term over a single oscillation period. For large Womersley numbers ($\alpha > 5$), the migration velocity increases near the channel walls ($d/l < 0.1$) and becomes negligible in the central region of the channel ($0.2 < d/l < 0.5$). The equilibrium focusing position can be located by determining the null point for each of the migration velocity profiles. The value $\alpha = 5$ is straightforward given that the undisturbed velocity profile (3.3) changes dramatically beyond this threshold. Less so is the null point, which moves closer to the wall with increasing α as a result of opposing effects (see figure 3a). Owing to increasing α , velocity

gradients become larger near the walls and smaller near the centreline (3.3). This implies that the wall interaction force becomes relatively stronger but is also confined closer to the wall. Note that results in figure 1(b) are not valid for $d/l \rightarrow 0$ and break down when $d/l \sim \kappa$, as this violates the assumed separation of scales between the outer and inner problems. The oscillatory flow-induced inertial lift on a sphere close to a wall has been addressed numerically by Fischer *et al.* (2004).

4. Experimental methods

Experiments were performed in a straight channel with a rectangular cross-section of high aspect ratio fabricated from a piece of aluminium sheet metal through wire electrical discharge machining. The total channel length L was 4 cm and the height was 2.5 mm. The channel walls were wet sanded to smoothness, resulting in a width l of 300 μm with $<0.2\%$ deviation from parallel plates along the channel length. The top and bottom walls of the channel were completed by adhering transparent packaging tape to the sheet metal. The tape was perforated at the channel inlet and outlet, and microfluidic tubing was inserted and sealed with epoxy.

The variable-frequency pulsatile flow in the microfluidic device was generated by combining a steady flow component with an oscillatory flow component. The steady flow component was generated at the inlet using a syringe pump. A volumetric flow rate of $20 \mu\text{l min}^{-1}$ was used throughout this study unless specified otherwise. For the given channel dimensions, this flow rate corresponded to a maximum flow speed $\bar{u}'_s = 0.54 \text{ mm s}^{-1}$. The oscillatory flow component was generated at the outlet using an oscillatory pressure signal generated by an external oscillatory driver. This was accomplished by interfacing the microfluidic tubing at the outlet to a loudspeaker diaphragm (Vishwanathan & Juarez 2020). The frequencies used here range over $25 \leq f \leq 500 \text{ Hz}$, with the angular frequency defined as $\omega = 2\pi f$. The maximum values of the oscillatory velocities ranged from 34 to 89 mm s^{-1} and were much larger than the steady flow velocity ($s\omega \gg \bar{u}'_s$).

Polystyrene particles were density-matched in an aqueous glycerol solution (23 % w/w) with density $\rho = 1060 \text{ kg m}^{-3}$ and kinematic viscosity $\nu = 1.687 \times 10^{-6} \text{ m}^2 \text{ s}^{-1}$. Three different suspensions with particle radii $a = 5.4, 8.1$ and $10.4 \mu\text{m}$ were used. Particle suspensions were in the dilute limit with volume fractions ranging from 0.02 % up to 0.05 %. Particles were imaged at the channel midplane (height) with bright-field microscopy using a $10\times$ objective lens with a depth of focus of $10 \mu\text{m}$. The acquisition frequency of 5 Hz and exposure time of 100 μs were used to monitor the rectified component of particle displacement. The imaging location was at the lengthwise centre of the channel, or 2 cm away from the inlet. The residence time of a particle is defined as the shortest time to travel from the inlet to the region of observation and is given by $t_R = L/2\bar{u}'_s = 37 \text{ s}$. However, during this time, the maximum total distance travelled by a particle will take into account the oscillatory component, since $s\omega \gg \bar{u}'_s$, and so it is estimated that $L_R = 4sf t_R$. Therefore, here L_R is referred to as the focusing distance travelled before observation and ranges from 0.8 to 2.1 m.

5. Experimental results

The dynamics of inertial focusing in planar pulsatile flows is qualitatively demonstrated in the space–time plot shown in figure 2(a). Here, suspended particle concentrations at each position along the channel width are represented in greyscale, where light

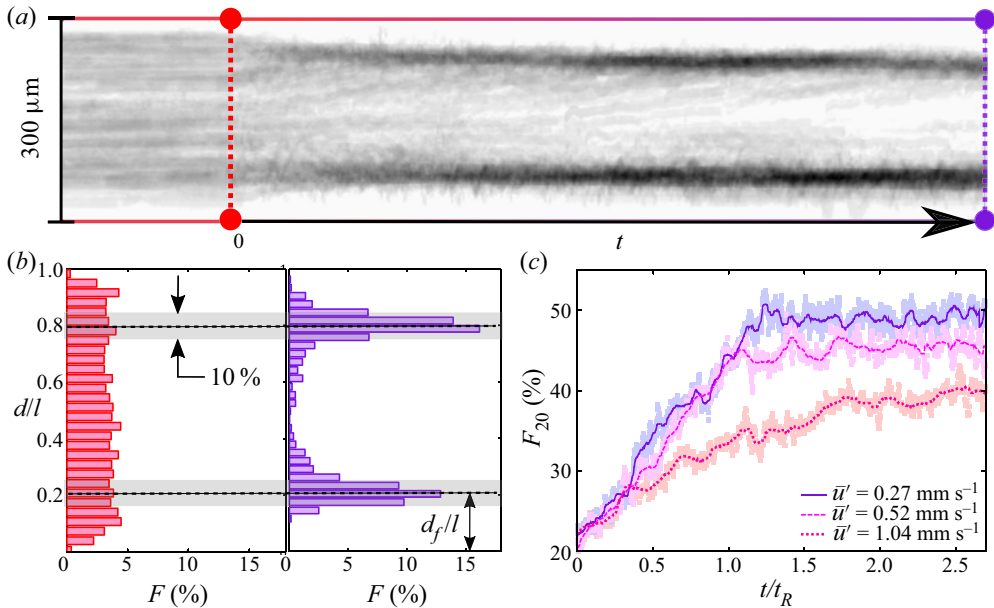


Figure 2. (a) Space–time plot of suspended particles migrating to equilibrium positions under pulsatile flow. (b) Histograms of the particle distribution along the channel width for (left) steady flow and (right) pulsatile flow. The focusing efficiency, denoted by F_{20} , quantifies the fraction of particles found within a distance $l/10$ of both focusing positions. (c) Transient focusing efficiency for different steady flow velocities. The efficiency reaches a steady value for all cases after $t/t_R > 1.5$.

grey corresponds to a low concentration of particles and dark grey corresponds to a high concentration of particles. Initially, particles are uniformly distributed along the spanwise direction, as they are transported by a purely steady unidirectional flow. After the oscillatory component is introduced ($t = 0$), concentration gradients emerge as particles migrate across streamlines and localize into two dark bands.

Histograms of particle positions along the channel width, obtained from digital particle identification and tracking techniques, quantitatively demonstrates the transformation from a uniformly dispersed suspension to a focused suspension, shown in figure 2(b). The particle number distributions are normalized by the total flux of particles observed. The peaks of the distribution correspond to the localization of particles after migration across streamlines. The peak positions are the measured equilibrium focusing positions, defined by their distance d_f/l from the channel walls. Since this measurement depends on the local width of the channel, particle tracking was used to extract the steady flow profile that was then fitted to a parabolic curve, whose fitting constants determine the precise centreline and local channel width. The focusing efficiency, denoted by F_{20} , quantifies the total fraction of particles located within a distance $l/10$ of both focusing positions and is indicated by the shaded band shown in figure 2(b). Therefore, F_{20} ranges from 20 %, corresponding to a uniformly dispersed suspension, up to 100 %, corresponding to the complete localization of particles at the focusing positions.

When observing a fixed position along the channel length, the steady flow component determines both the absolute time required for the particle distribution to reach steady state and the eventual focusing efficiency. For example, the focusing efficiency for $\alpha = 4$, $\kappa = 0.018$, $Re_p = 0.014$ and the steady flow speeds \bar{u}'_s of 0.27, 0.52 and 1.04 mm s⁻¹ initially starts from 20 % and increases with time, as shown in figure 2(c). The residence

times t_R associated with the steady flow speeds are 74, 37 and 18.5 s, respectively. The rate of increase in the focusing efficiency is initially identical for all steady flow speeds and approaches zero by $t/t_R = 1.5$. As expected, the steady state F_{20} increases with residence time due to the larger focusing length travelled and reaches maximum values of 50 %, 45 % and 40 %, respectively.

The focusing positions and focusing efficiency are measured only after the particle distributions reach a steady state. Henceforth, the data presented will correspond to a steady state with a steady flow speed of $\bar{u}'_s = 0.54 \text{ mm s}^{-1}$ with a residence time of $t_R = 37 \text{ s}$. To ensure steady state, measurements are only made after pulsatile flow is applied for 100 s ($t/t_R > 2.5$), after which the particle distribution is measured and synthesized over another 100 s interval. The data (symbols) for focusing position and focusing efficiency are mean values (multiple experiments and time-averaged during the 100 s interval). The coloured regions represent the error, estimated here as half of the maximum difference of any measurement from the mean. For example, the comparison between instantaneous values and mean value are evident in [figure 2\(c\)](#).

The focusing positions d_f/l approach the channel wall as the Womersley number increases above $\alpha > 5$, as shown in [figure 3\(a\)](#). For small κ , there is good agreement between experimental measurements ($\kappa < 0.02$) and theory ($\kappa = 0$), as indicated by the dashed line. The theoretical focusing positions are determined by null points in the migration velocity curves, shown in [figure 1\(b\)](#). For large κ , the deviation of experimental measurements ($\kappa > 0.02$) from theory ($\kappa = 0$) increases with particle size. The corresponding focusing position for a given Womersley number occurs farther away from the channel wall, while preserving the qualitative theoretical ($\kappa = 0$) trend. That is, the focusing positions continue to approach the channel wall for Womersley numbers above $\alpha > 5$. While the focusing position can be described quite accurately with advanced computational methods for an individual particle, the evaluation of focusing efficiency requires a comprehensive statistical analysis of particle positions for many particles across all initial conditions. This is made possible only with an experimental approach.

The focusing efficiency was measured for different particle sizes and Womersley numbers, shown in [figure 3\(b\)](#). Here, the focusing length of $L_R = 2.1 \text{ m}$ was maintained across frequencies by independently adjusting the amplitude and frequency such that the product of the oscillatory velocity magnitude ($s\omega$) is equal to a constant. For small Womersley numbers ($\alpha < 5$), the focusing efficiency ranges from 50 % to 90 % for the particle Reynolds numbers of 0.01 and 0.07, respectively. The high extent of focusing efficiency, $F_{20} > 80 \%$ for $Re_p = 0.071$, illustrates the effectiveness of oscillatory flows for inertial focusing. For large Womersley numbers ($\alpha > 5$), the focusing efficiency decreases monotonically and approaches 20 %, or that of a uniformly dispersed suspension, for the smallest particle size.

The focusing efficiency was also measured for different oscillatory amplitudes and Womersley numbers, shown in [figure 3\(c\)](#). Here, the relative particle size of $\kappa = 0.035$ was maintained constant throughout. Once again, for small Womersley numbers ($\alpha < 5$), the focusing efficiency has a similar range of 45 % to 90 % for the oscillatory velocities of 34 and 89 mm s^{-1} , respectively. For large Womersley numbers ($\alpha > 5$), the focusing efficiency decreases monotonically and approaches 20 % for the lowest oscillatory amplitude. From both cases, for a fixed Womersley number, a larger $s\omega$ or κ value determined a higher extent in the F_{20} value, in agreement with inertial focusing in steady flows.

A distinct advantage of studying inertial focusing in oscillatory flows compared to focusing in steady flows is that the migration of individual particles across a large resident

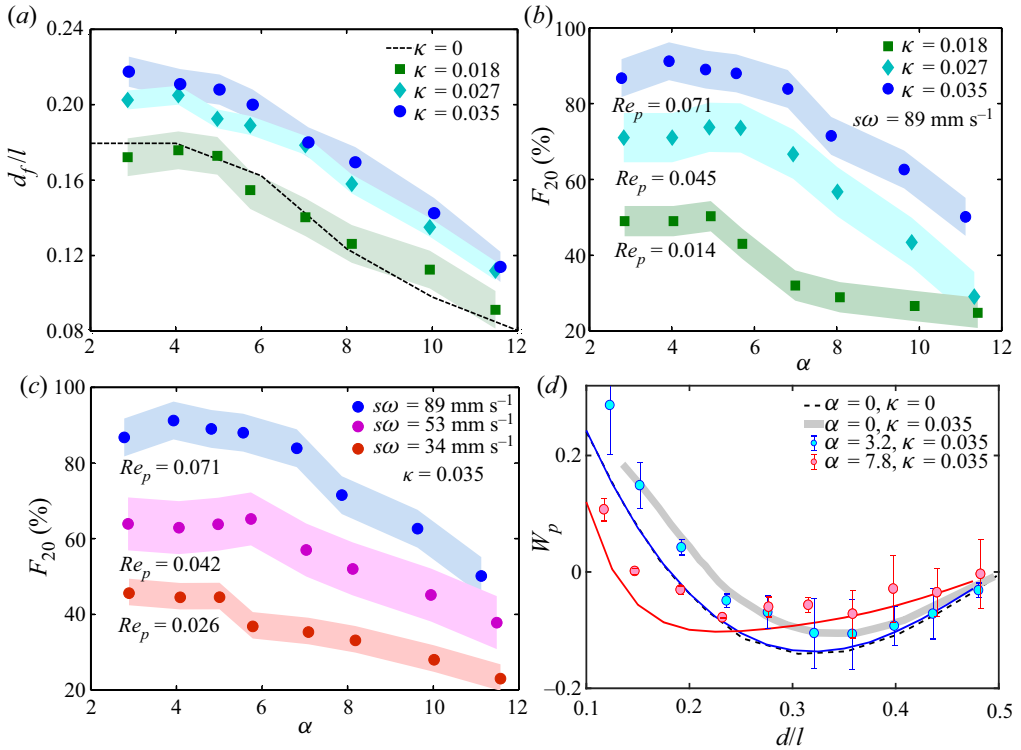


Figure 3. (a) The focusing position for different relative particle sizes as a function of Womersley number. The experimental measurements (symbols) are similar to the analytical predictions (dashed) obtained from figure 1(b). The discrepancy is due to finite particle size ($\kappa > 0.02$). (b) The focusing efficiency for suspensions of different relative particle sizes as a function of Womersley number. The oscillatory velocity amplitude ($s\omega$) is maintained constant across throughout. (c) The focusing efficiency for a suspension of a fixed particle size as a function of the Womersley number for varying oscillatory velocity amplitude. The oscillatory velocity amplitude is kept constant for a single curve but varied across curves. (d) The migration velocity profile for a low (blue) and high (red) Womersley number. The experimental measurements (symbols) are compared to corresponding theoretical results for point particles in an oscillatory flow (red solid and blue solid, (3.18) and (3.19)), as well as being compared to point (black dashed) and finite-size (grey stripe; Asmolov *et al.* 2018) particles in a steady flow.

path length can be clearly observed and tracked. Therefore, it is possible to accurately measure the average migration velocity profile across the channel width, something that is not easily achieved in steady flows due to practical constraints of resolving single particles over a large field of view. The guiding principle is, once again, the decoupling of travelled distance from displacement (Vishwanathan & Juarez 2020). The averaged migration velocity at each spanwise position for a low-frequency ($\alpha = 3.2$) and a high-frequency ($\alpha = 7.8$) pulsatile flow and relative particle size of $\kappa = 0.035$ is shown in figure 3(d). The migration velocity was measured by tracking the position of many individual particles ($N \approx 100\text{--}1000$ per experiment) during the transient regime, i.e. $t/t_R < 1$ in figure 2(c). Experimental measurements (symbols) compare well with analytical results for point particles (solid, (3.18) and (3.19)) in an oscillatory flow. Here, symbols represent average values and error bars represent one standard deviation from the mean. A precise match with half the magnitude of numerical results for finite-sized particles (grey stripe,

$\kappa = 0.035$; Asmolov *et al.* 2018) in a steady flow is observed for the low-frequency case. See the comment about the numerical factor of 1/2 in § 3.3.

6. Discussion

The Womersley number is an important parameter for pulsatile flows (Dincau, Dressaire & Sauret 2019). It defines the ratio of the channel width to the Stokes boundary layer thickness, and determines the velocity profile for unsteady laminar flows. While inertial focusing in pulsatile flows provides an opportunity for reduced channel lengths and pressure drops in biomedical applications, it first requires understanding the direct link between transient inertial forces and particle migration velocity profiles in unsteady laminar flows.

In general, the focusing efficiency is independent of α for small Womersley numbers ($\alpha < 5$), as shown in figures 3(b) and 3(c). The constant focusing efficiency for these cases is due to the migration velocity profiles, which are also independent for $0 < \alpha < 5$, as shown in figure 1(b). However, for large Womersley numbers ($\alpha > 5$), the focusing efficiency decreased monotonically with increasing α , as shown in figures 3(b) and 3(c). The decrease in the focusing efficiency for these cases is due to the migration velocity profiles, which become increasingly weak at the centre of the channel for $\alpha > 5$, as shown in figure 1(b).

For focusing in steady laminar flows, the particle Reynolds number determines the magnitude of the particle migration velocity, that is, a larger Re_p corresponds to increased focusing efficiency. In contrast, $Re_p = \kappa^2 \alpha^2 / St$ does not always directly correlate with improved focusing efficiency in unsteady oscillatory flows. In fact, above a critical Womersley number ($\alpha > 5$), the focusing efficiency decreases with increasing Re_p if only α is increased. Therefore, for the purposes of inertial particle focusing, it is best to maintain $\alpha < 5$. For $\alpha > 5$, although the focusing efficiency decreases, the migration velocity profile suggests that particles migrate away from the channel wall with speeds that increase directly with Womersley number. This effect could be leveraged in efforts to mitigate the fouling of surfaces without affecting the bulk concentration profile.

Acknowledgements. We thank M. Garcia, I.C. Christov and G.J. Elfring for critical discussions and feedback on initial versions of this paper.

Acknowledgements. The authors report no conflict of interest.

Author ORCIDs.

 Giridar Vishwanathan <https://orcid.org/0000-0002-3737-3754>;

 Gabriel Juarez <https://orcid.org/0000-0002-5854-6925>.

REFERENCES

- ASMOLOV, E.S. 1999 The inertial lift on a spherical particle in a plane poiseuille flow at large channel Reynolds number. *J. Fluid Mech.* **381**, 63–87.
- ASMOLOV, E.S., DUBOV, A.L., NIZKAYA, T.V., HARTING, J. & VINOGRADOVA, O.I. 2018 Inertial focusing of finite-size particles in microchannels. *J. Fluid Mech.* **840**, 613–630.
- ASMOLOV, E.S. & MCLAUGHLIN, J.B. 1999 The inertial lift on an oscillating sphere in a linear shear flow. *Intl J. Multiphase Flow* **25** (4), 739–751.
- COIMBRA, C.F.M. & KOBAYASHI, M.H. 2002 On the viscous motion of a small particle in a rotating cylinder. *J. Fluid Mech.* **469**, 257–286.
- DI CARLO, D. 2009 Inertial microfluidics. *Lab on a Chip* **9**, 3038–3046.
- DI CARLO, D., IRIMIA, D., TOMPKINS, R.G. & TONER, M. 2007 Continuous inertial focusing, ordering, and separation of particles in microchannels. *Proc. Natl Acad. Sci. USA* **104**, 18892–18897.

- DINCAU, B., DRESSAIRE, E. & SAURET, A. 2019 Pulsatile flow in microfluidic systems. *Small* **16** (9), 1904032.
- FISCHER, P.F., LEAF, G.K. & RESTREPO, J.M. 2002 Forces on particles in oscillatory boundary layers. *J. Fluid Mech.* **468**, 327–347.
- FISCHER, P.F., LEAF, G.K. & RESTREPO, J.M. 2004 Influence of wall proximity on the lift and drag of a particle in an oscillatory flow. *Trans. ASME J. Fluids Engng* **127** (3), 583–594.
- HO, B.P. & LEAL, L.G. 1974 Inertial migration of rigid spheres in two-dimensional unidirectional flows. *J. Fluid Mech.* **65** (2), 365–400.
- MARTEL, J.M. & TONER, M. 2014 Inertial focusing in microfluidics. *Annu. Rev. Biomed. Engng* **16**, 371–396.
- MIYAZAKI, K., BEDEAUX, D. & AVALOS, J.B. 1995 Drag on a sphere in slow shear flow. *J. Fluid Mech.* **296**, 373–390.
- MORITA, Y., ITANO, T. & SUGIHARA-SEKI, M. 2017 Equilibrium radial positions of neutrally buoyant spherical particles over the circular cross-section in Poiseuille flow. *J. Fluid Mech.* **813**, 750–767.
- MUTLU, B.R., EDD, J.F. & TONER, M. 2018 Oscillatory inertial focusing in infinite microchannels. *Proc. Natl Acad. Sci. USA* **115**, 7682–7687.
- SCHONBERG, J.A. & HINCH, E.J. 1989 Inertial migration of a sphere in Poiseuille flow. *J. Fluid Mech.* **203**, 517–524.
- SEGRÉ, G. & SILBERBERG, A. 1961 Radial particle displacements in Poiseuille flow of suspensions. *Nature* **189**, 209–210.
- SHI, P. & RZEHAŁ, R. 2020 Lift forces on solid spherical particles in wall-bounded flows. *Chem. Engng Sci.* **211**, 115264.
- STOECKLEIN, D. & DI CARLO, D. 2019 Nonlinear microfluidics. *Anal. Chem.* **91**, 296–314.
- VISHWANATHAN, G. & JUAREZ, G. 2020 Generation and application of sub-kilohertz oscillatory flows in microchannels. *Microfluid Nanofluid* **24**, 1–10.
- WAKABA, L. & BALACHANDAR, S. 2005 History force on a sphere in a weak linear shear flow. *Intl J. Multiphase Flow* **31** (9), 996–1014.